remote sensing

MDPI

Article

Regional Models for Sentinel-2/MSI Imagery of Chlorophyll *a* and TSS, Obtained for Oligotrophic Issyk-Kul Lake Using High-Resolution LIF LiDAR Data

Vadim Pelevin [1,*], Ekaterina Koltsova [2], Aleksandr Molkov [3,4], Sergei Fedorov [5], Salmor Alymkulov [6], Boris Konovalov [1], Mairam Alymkulova [6] and Kubanychbek Jumaliev [7]

1 Shirshov Institute of Oceanology, 36 Nakhimovsky Prospekt, Moscow 117997, Russia; konovalov.bv@ocean.ru
2 Moscow Institute of Physics and Technology, 9 Institutskiy Per., Dolgoprudny 141700, Russia; koltsova.es@phystech.edu
3 Laboratory of Hydrology and Ecology of Inland Waters, Lobachevsky State University of Nizhny Novgorod, 23 Gagarin Avenue, Nizhny Novgorod 603022, Russia; molkov@ipfran.ru
4 Institute of Applied Physics of the Russian Academy of Sciences, 46 Ulyanov St., Nizhny Novgorod 603950, Russia
5 Marine Hydrophysical Institute of the Russian Academy of Sciences, 2 Kapitanskaya St., Sevastopol 299011, Russia; s.fedorov@mhi-ras.ru
6 Department of Informatics and Computer Science, Razzakov Kyrgyz State Technical University, Str. Aitmatova 66, Bishkek 720044, Kyrgyzstan; salmor55@kstu.kg (S.A.); malymkulova@kstu.kg (M.A.)
7 Department of Natural Sciences, International Medical University, Str. Ankara 1/17, Bishkek 720048, Kyrgyzstan; thescience@imu.edu.kg
* Correspondence: pelevin@ocean.ru

Abstract: The development of regional satellite bio-optical models for natural waters with high temporal and spatial variability, such as inland seas, reservoirs, and coastal ocean waters, requires the implementation of an intermediate measuring link in the chain, "water sampling—bio-optical models", and this link must have certain intermediate characteristics. The most crucial of them are the high-precision measurements of the main water quality parameters, such as the concentration of chlorophyll *a* (Chl *a*), colored dissolved organic matter (CDOM), and total suspended sediments (TSS) in the upper water layer, together with a high operational rate and the ability to cover a large water area in a short time, which corresponds to a satellite overpass. A possible solution is to utilize laser-induced fluorescence (LIF) of water constituents measured by a marine LiDAR in situ with a high sampling rate from a high-speed vessel. This allows obtaining a large ground-truth dataset of the main water quality parameters simultaneously with the satellite overpass within the time interval determined by NASA protocols. This method was successfully applied to the oligotrophic Issyk-Kul Lake in Kyrgyzstan, where we obtained more than 4000 and 1000 matchups for the Chl *a* and TSS, respectively. New preliminary regional bio-optical models were developed on the basis of a one-day survey and tested for archive Sentinel-2A data for 2022. This approach can be applied for regular monitoring and further correction in accordance with seasonal variability. The obtained results, together with previously published similar studies for eutrophic coastal and productive inland waters, emphasize the applicability of the presented method for the development or adjustment of regional bio-optical models for water bodies of a wide trophic range.

Keywords: Sentinel; LIF; LiDAR; chlorophyll; TSS; bio-optical models; ocean color; Issyk-Kul Lake

Citation: Pelevin, V.; Koltsova, E.; Molkov, A.; Fedorov, S.; Alymkulov, S.; Konovalov, B.; Alymkulova, M.; Jumaliev, K. Regional Models for Sentinel-2/MSI Imagery of Chlorophyll *a* and TSS, Obtained for Oligotrophic Issyk-Kul Lake Using High-Resolution LIF LiDAR Data. *Remote Sens.* **2023**, *15*, 4443. https://doi.org/10.3390/rs15184443

Academic Editor: SeungHyun Son

Received: 15 July 2023
Revised: 28 August 2023
Accepted: 7 September 2023
Published: 9 September 2023

1. Introduction

Ocean color sensors are an indispensable tool for regular and global monitoring of any water, especially due to their high spatial resolution, global coverage, free availability, reliability, and good measurement repeatability. From year to year, different countries produce the latest sensors, which confirms the rapid growth and progress in this field

of applied science. Sentinel-2/MSI and Sentinel-3/OLCI images are currently widely used for remote sensing of inland freshwater reservoirs [1–4]. Their spatial resolution and set of spectral bands are suitable for monitoring optically complex waters, including hypereutrophic ones. However, without exaggeration, dozens of other satellite instruments already operating and preparing to launch compete with them. All these missions face the same problem, namely, the refinement of the atmospheric correction algorithms as well as the improvement of existing or the development of new bio-optical models to obtain the main water quality parameters. The latter include, but are not limited to, the concentrations of chlorophyll *a* (Chl *a*), colored dissolved organic matter (CDOM), and total suspended sediments (TSS).

There are many bio-optical models for obtaining these parameters in the upper quasi-homogeneous water layer of lakes and inland seas. However, as previous studies, including ours, have shown, the models require validation due to systematic errors in productive waters [1,2,5,6].

This paper is devoted to the study of this issue for oligotrophic waters using the example of the high-altitude Issyk-Kul Lake in Kyrgyzstan, which today requires close attention. This lake (42.25°N, 77.15°E) is located between the Northern Tian Shan Mountains at an altitude of 1608 m. The lake is 182 km long and 60 km wide (Figure 1). The maximum depth is 686 m, ranking sixth in the list of the deepest lakes in the world. The lake is brackish, and the average water salinity is 5.9‰. The name of the lake, in translation from the Kyrgyz language, means "warm lake", since the lake does not freeze in winter, even at negative temperatures of the continental climate. An attempt to explain this phenomenon was made in [7,8]. 118 rivers and streams flow into the lake, and not a single river flows out of it. The largest rivers are the Jyrgalang, Tup, and Karakol. All rivers significantly change the water transparency both in the mouth and coastal area, as well as in the open lake during the season of snowmelt or heavy rains. As a result, these areas have a high spatiotemporal variability of the water's optical properties, and we will show this below.

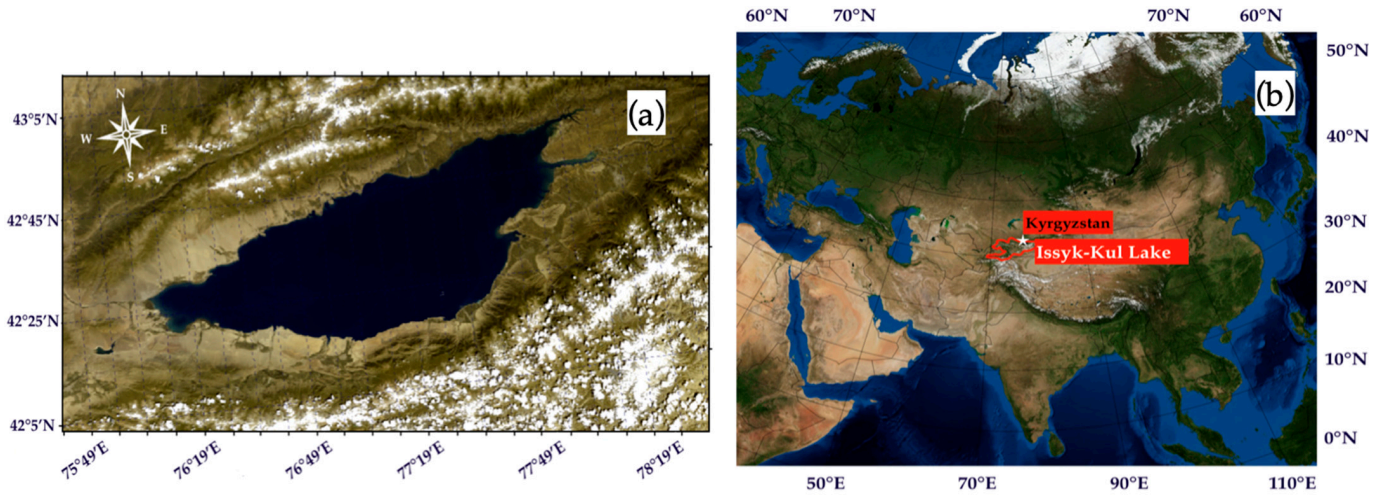

Figure 1. Issyk-Kul Lake: (**a**) location on the world map (NASA "Blue Marble" image (https://visibleearth.nasa.gov/collection/1484/blue-marble, accessed on 1 August 2023) and (**b**) the satellite RGB-composite image (Sentinel-3B, accessed on 17 July 2022).

Issyk-Kul Lake welcomes about a million tourists from all over the world every year. At the same time, the recreational potential of the lake is far from being exhausted, and there are plans to increase the tourist flow in the coming decades, which will inevitably lead to the growth of coastal development and pollution of the coastal areas. This poses a threat to the ecological state of the lake, which is aggravated by the presence of mining and chemical industries in the lake drainage basin. Cases of man-made disasters are already known [8]. At the same time, it should be noted that retrospective information on the

ecological state of the lake is fragmentary [8]. Comprehensive studies of hydrophysics, hydrochemistry, hydro-optics, bathymetry, and methane release throughout the whole lake, including the large tributaries, were conducted jointly by scientists from Russia, Germany, and Kyrgyzstan in the period from 2014 to 2019 [7,9–11].

However, with a sufficient number of clear days throughout the year, the use of satellite data as a regular instrument for monitoring the water quality in the lake seems to be rational and effective. Moreover, the significant spatial scale of Issyk-Kul Lake makes it possible to use all satellite information with any spatial resolution. However, it is necessary to employ high-resolution satellite data, such as Sentinel-2/MSI, to study the effect of inflows. Although two satellites (A and B) were launched relatively recently (in 2015 and 2017), a whole series of studies aimed at examining their applicability for monitoring the water quality of inland waters, for example [1,3,4,12–15], have already been published.

Most existing bio-optical models were built using in situ data from several dozen stations under the assumption that the temporal variability of the optical properties of water is negligible. However, according to some papers, e.g., [16–18], it is difficult to consider this condition to be true, especially since its confirmation (or, conversely, refutation) is not given at all. In this context and in relation to regions with strong surface currents, remote sensing of the upper water layer by laser-induced fluorescence (LIF) LiDAR from a fast-moving vessel is an effective tool for collecting ground-truth data on water constituents simultaneously with the satellite overpass [6]. This layer makes the main contribution to the water-leaving signal registered by ship or satellite radiometers. Marine LIF LiDAR (Light Detection and Ranging) measures the main water quality parameters (Chl *a*, TSS, and CDOM) with a high sampling rate, excluding the effect of sampling on the accuracy of the final result and providing information on the average concentration of water constituents in a column of 0.5–5 m, depending on turbidity. The absolute error of TSS and Chl *a* in the case of using, for example, our UFL-9 LiDAR (see information below) does not exceed 10% and 16%, respectively [6,19]. As our experience shows, the mineral component of the suspended hydrosol, which makes the main contribution to the laser backscatter signal, is registered by LiDAR and also usually prevails in a mass of the total suspension. Therefore, hereafter, we use the term TSS to refer to the total suspended solids.

Fluorescence LiDARs have successfully been used over the past few decades by research teams from different countries. In recent years, these technologies have made a qualitative breakthrough due to the significant development of the instrument base and the accumulation of extensive experience in the use of marine LiDARs. For environmental monitoring and scientific research, fluorescent LiDARs are usually employed from ships or aircraft to measure the concentrations of Chl *a* and CDOM in different waters of the World Ocean: the Atlantic Ocean [10,20], the Black Sea [21,22], the Arctic Ocean [23,24], the Baltic Sea [25], the Southern Ocean [26], and the South China Sea [27]. There are also examples of LIF LiDAR used to measure suspension concentration in water [21,28,29]. For productive and turbid inland waters, such LiDARs are used much less frequently, but with the advent of smart and portable LiDARs, such studies are being carried out more often [30–32].

Due to the high compatibility of the spatial and temporal scales with satellite imaging, LIF LiDAR sensing is regularly employed to develop and validate satellite radiometric bio-optical models. For example, in [33], the LIF LiDAR measurements of Chl *a* were implemented simultaneously with SeaWiFS and MODIS satellites in the Antarctic, Pacific, and Indian Oceans. In [34], CDOM product data for SeaWiFS was calibrated by LiDAR data for the Antarctic Ocean. In [20], MODIS Terra data on Chl *a* concentration were verified using aviation fluorescence LiDAR in the Atlantic Ocean. In [35], Chl *a* LiDAR data in the Yellow Sea were compared with MODIS products. In [2], the LiDAR and MODIS Terra data of Chl *a*, CDOM, and TSS were compared for Lake Balaton in Hungary. In [31], measurements of Chl *a* and CDOM were conducted on Qiandao Lake (China) for MODIS. The results of the successful verification of Sentinel-2/MSI data to retrieve the concentration of Chl *a* and TSS in the highly productive Gorky Reservoir were published in [2]. Thus, all the above-mentioned studies show the advantages of using fluorescence marine LiDARs

for the verification of satellite data for a wide range of water types. This paper continues our team's research aimed at the development of bio-optical models for various inland waters, namely the high-altitude oligotrophic Issyk-Kul Lake of Kyrgyzstan. The water optical properties of the open part of the lake are similar to those of open ocean waters, with concentrations of Chl *a* significantly less than 1 µg/L and mineral-suspended matter less than 1 mg/L. However, in the estuarine areas, these values are significantly higher. The models presented in this paper, being the first approximation, serve as a starting point for regular monitoring of the water quality of Issyk-Kul Lake using high-resolution satellite data from Sentinel-2/MSI. To date, the relevant regional models have not been presented in the literature.

2. Materials and Methods

2.1. Study Region

In situ measurements were conducted on 16 July 2022, in the eastern part of the lake, which is subject to significant runoff from the large tributaries, such as the Tyup, Jergalan, and Karakol Rivers (Figure 2). The regions outside their mouths are characterized by complex bathymetry with depths of 1–30 m, sand bottoms, and clear water (Secchi depth is about 15–18 m); therefore, the bottom near the coastline is clearly visible on satellite images. For this reason, certain regions were excluded from consideration. However, one of the features of the lake is the presence of underwater canyons, i.e., palaeochannels of the Tyup and Jergalan Rivers, extending for a considerable distance from the mouths. These palaeochannels are 2–3 km wide and 60–90 m deep [10], which is many times greater than the Secchi depth (less than 5 m for this region). Therefore, the bottom is invisible here, and we trust the data from the ship and satellite sensor due to the considerable depth and lack of the bottom effect. Inside the mouths and upstream, the water was much more turbid, i.e., the Secchi depth reached 1 m or even less. Figure 3a–c provides images of typical examples of the regions under study.

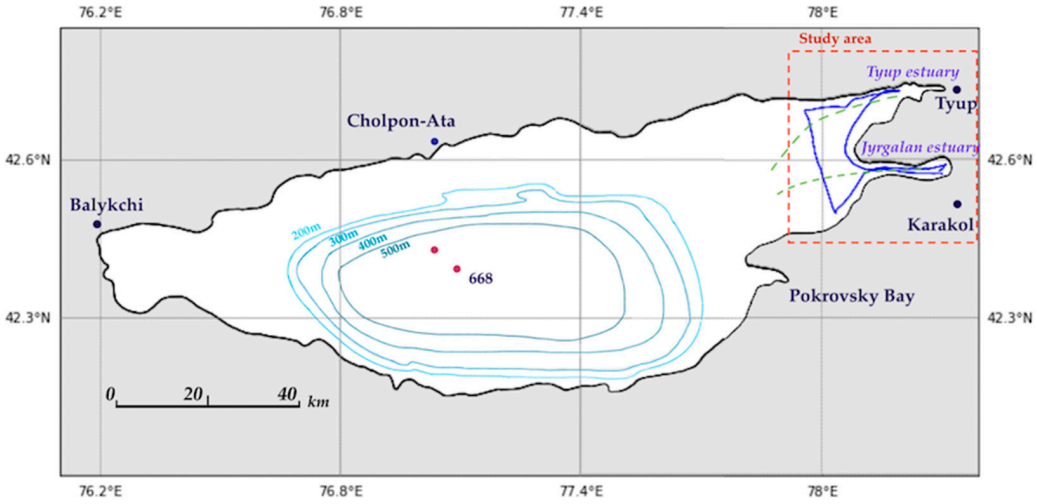

Figure 2. Map of Issyk-Kul Lake (https://matplotlib.org/basemap/, accessed on 20 December 2022) with schematized bathymetry contours of 200, 300, 400, and 500 m [7]. The red dots denote the deepest areas. The green dashed lines in the eastern part of the lake indicate the palaeochanels of the Jyrgalan and Tyup Rivers. The dark blue line in the eastern part of the lake is a ship path.

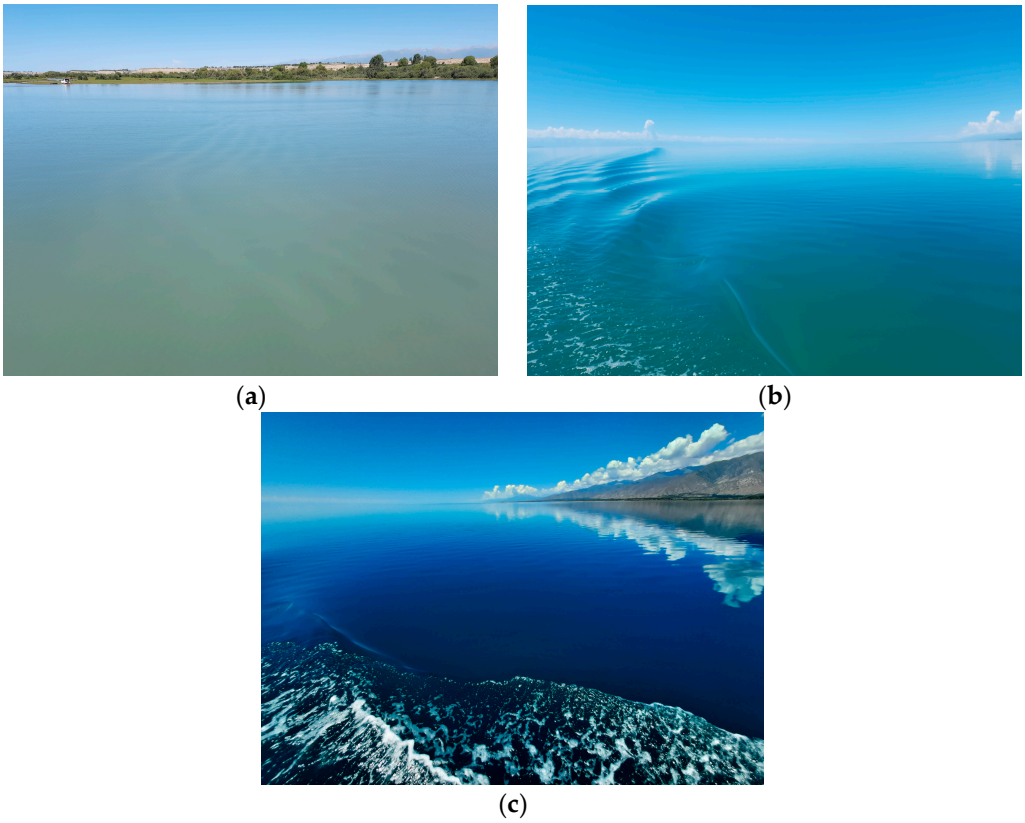

Figure 3. Photos of the studied region from a motorboat: (**a**) highly turbid waters of Jyrgalan River, (**b**) Tyup River, and (**c**) clean waters of the open lake between Jyrgalan and Tyup mouths.

The in situ measurements start at 08:12 local time (UTC+6) and end at 18:10 (UTC+6). The time of the satellite overpass was 11:36 (UTC+6). Measurements were performed with a light westerly wind of 3–4 m/s with its amplification up to 8 m/s at the moment of the satellite overpass. Measurements were performed from a thirteen-meter-long boat of the "Admiralteets" type, moving at a cruising speed of 4 m/s.

2.2. Field Measurements

Field measurements consisted of simultaneous LIF LiDAR and radiometric measurements from a moving motorboat in accordance with the approach [36,37] and water sampling for the LIF LiDAR calibration. The purpose of the LiDAR study was to obtain data on concentrations of Chl *a* and TSM in thousands of points throughout the studied region under the Sentinel-2/MSI overpass. LiDAR UFL-9 [30] was mounted onto the bow railing and oriented at an angle of 30° and 45° to the nadir and motion direction for sensing the undisturbed water column in front of the motorboat (Figure 4). By emitting an ultraviolet (355 nm) impulse twice per second, LiDAR UFL-9 registered the backward signals from the water column simultaneously at 8 wavelengths. In this paper, we considered time series only at two wavelengths of 355 nm and 685 nm, normalized by Raman scattering at 404 nm. The obtained signals describe TSS and Chl *a* distribution in Raman units along the motorboat path with a spatial resolution of 2 m. Their conversion into concentration units was performed after the expedition. For this purpose, we compared the fluorescence signals at the moment and at the water sampling site with the concentrations retrieved by the water samples in the laboratory. The samples were taken with a bucket from a stationary motorboat near the area sensing by LiDAR, then poured into plastic bottles with a volume of 5 land filtered through Whatman GF/F 0.7 μm pore filters. The collected filters were well-dried and transported to the laboratory. In the laboratory, the concentrations of Chl *a* and TSS were determined using the spectrophotometric method [38,39].

Figure 4. The ultraviolet fluorescence LiDAR UFL-9 on the motorboat.

To cover the widest possible range of variability in the water optical properties, the samples were taken along the entire motorboat path at 35 points with different visual turbidity and/or by strong variations of online LiDAR signals. As a result, the following calibration matches were obtained (Figure 5):

$$\text{Chl } a = 0.2083\ x_{685} - 0.0012,\ R^2 = 0.95, \quad (1)$$

$$\text{TSS} = 0.056\ x_{355} + 0.396,\ R^2 = 0.98, \quad (2)$$

where x_{685} and x_{355} are the LiDAR signals at 685 nm and 355 nm in Raman units, respectively, and R^2 is the determination coefficient.

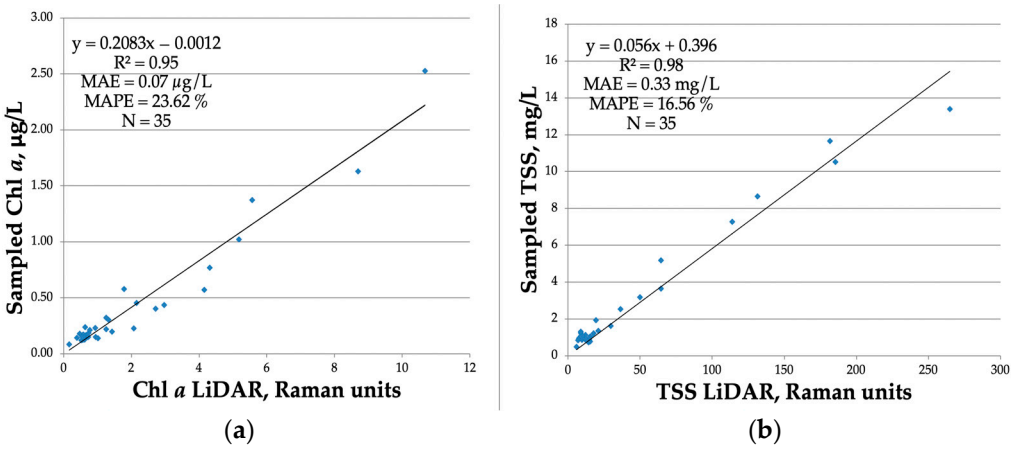

Figure 5. Results of comparison of LiDAR signals at stations and water samples analyzed in the laboratory according to concentrations of (**a**) Chl *a* and (**b**) TSS. Black lines correspond to the best calibration matches (1) and (2), respectively.

Radiometric measurements included above-water measurements of the directional upwelling radiance L_u, the sky radiance L_r, and the downwelling irradiance E_d using three Ocean Optics STS spectrometers with a spectral range of 400–750 nm, a spectral resolution of 1 nm, and a frequency of 1 Hz from a moving vessel. They were oriented to the water surface and relative to the Sun in accordance with the NASA protocol [40] for each straight-line course. After the course change, the spectrometers were rotated mechanically to get the correct angle with respect to the Sun. Paths with frequent tacking and turns were excluded from consideration.

The obtained time series of L_u, L_r, and E_d were smoothed by the median filter. After that, the remote sensing reflectance R_{rs} was calculated for each measurement (for every second) similarly to Mobley [41]:

$$R_{rs} = \frac{L_u - \rho \cdot L_r}{E_d}, \quad (3)$$

where $\rho = 0.0256 + 0.00039 \cdot w + 0.000034 \cdot w^2$, w is the wind speed. All R_{rs} falling into one pixel were averaged and the same for all pixels.

2.3. Sentinel-2/MSI Imagery and Image Processing

2.3.1. Match-Ups for Satellite Validation and Spatial-Temporal Variability within a Pixel

The Sentinel-2/MSI image, dated 16 July 2022, was downloaded from the website of the European Space Agency (https://scihub.copernicus.eu, accessed on 20 November 2022). Level-2 data with a spatial resolution of 10 m was used to calculate the water bio-optical parameters. The satellite overpass time was 11:36 a.m. local time (UTC+6). Some results of assessment of the Sentinel-2/MSI products accuracy are given in the Appendix A.

In just one working day, more than 47,000 LiDAR and 28,000 radiometric measurements were received (from 8:12 to 18:00 local time). In order to compare full-scale measurements with satellite data, the in situ data were filtered both by time (with allowance for the permissible time interval of ±3 h, according to NASA protocols, https://seabass.gsfc.nasa.gov/wiki/validation_description, accessed on 20 November 2022) and by the studied regions (see below).

Data filtering for Chl *a* and TSS was performed in several stages. First of all, radiometric and LiDAR data were synchronized since the LiDAR and spectrometers have different temporal resolutions, namely, 2 Hz and 1 Hz, respectively. Furthermore, both datasets were averaged within each satellite pixel. Depending on the direction and speed of the vessel, from 2 to 7 measurements fell into one pixel. As a result, a final dataset of in situ measurements (Chl-*a*, TSS, and Rrs) corresponding to about 7000 satellite pixels was obtained.

After that, we excluded from consideration those sections of the vessel's path that correspond to shallow water (Figure 6). For this purpose, we use the B3 band (560 nm), where the bottom is clearly visible. As a result, 4111 synchronous pairs of satellite data and in situ measurements were accepted. In addition, in order to improve the results of estimating TSS concentration via satellite data, the authors decided to additionally reject outlier data. This rejection was carried out through the analysis of the linear correlation between TSS concentration measured by the LiDAR and the in situ remote sensing reflectance R_{rs} at a wavelength of 560 nm within a 95% confidence interval. Values not included in this interval were excluded from consideration. Such filtering made it possible to take into account the insufficient sensitivity of the MSI satellite sensor for the low-concentration regions, as well as errors in the Sentinel-2B/MSI Level 2 product atmospheric correction algorithm, which inevitably occur when using single-channel algorithms. The resulting dataset was then superimposed on the satellite image for additional data rejection using the linear correlation between the TSS concentration measured by the LiDAR and the spectral radiance coefficient at the bottom of the atmosphere ρ_{BOA} at the same wavelength of 560 nm (B3 band). As a result, 1071 pairs of in situ and satellite data were obtained to evaluate the TSS models and 4111 pairs for Chl *a*. All further data processing was performed using Python.

Figure 6a shows the division of the vessel path into zones: zone 1 (blue) corresponds to the region with outflows from the Jergalan River, which are highlighted in the satellite image; zone 2 (red) corresponds to the region with partial bottom influence, at the end of which the satellite overpass took place (marked with the satellite logo); zone 3 (green) corresponds to the region with pronounced optical influence of the bottom; zone 4 (purple) corresponds to the region with deep water zone and very low concentrations of Chl *a* and TSS; zone 5 (orange) and zone 6 (dark blue) were excluded from consideration due to non-compliance with NASA's protocols on the permissible time interval for validation of

satellite data. The authors added zone 7 (light green), which corresponds to the inflows of the Tyup River. Figure 6b,c demonstrate the results of filtering the data on the path and show the parts of the tracks that were used to develop regional models for Chl *a* (Figure 6b) and TSS (Figure 6c).

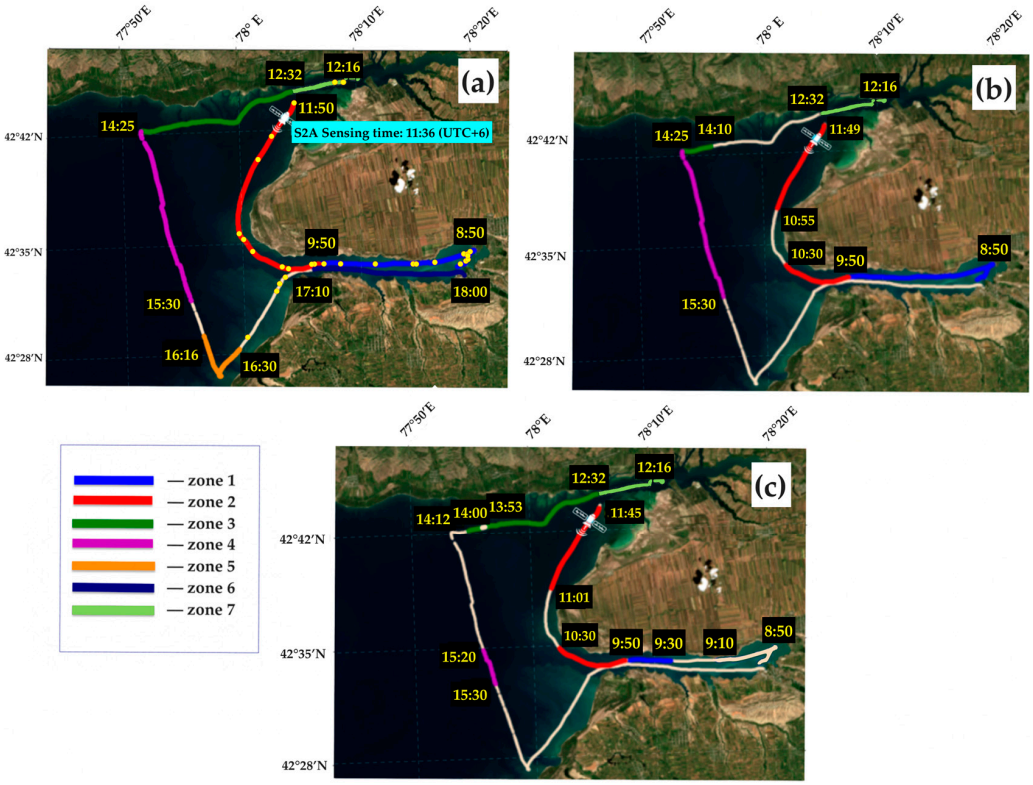

Figure 6. The RGB-composite image of Issyk-Kul Lake: (**a**) basic map with the motorboat path divided into water zones with river outflows (blue (1), dark blue (6), and light green (7) colors), shore water zones (red (2), green (3), and orange (5) colors), and zone with deep water (purple (4) color), yellow dots represent stations, (**b**) map with filtered data for Chl *a* estimation, and (**c**) map with filtered data for TSS estimation. The white satellite logo represents the moment of the Sentinel-2A overpass (11:36 a.m. local time (UTC+6)).

2.3.2. Accuracy Metrics

The model's accuracy was estimated by the mean absolute percent error (*MAPE*), the mean absolute error (*MAE*), and the root-mean-square error (*RMSE)*:

$$MAPE = \frac{1}{N}\sum_{i=1}^{N}\frac{\left|y_i^{est} - y_i^{obs}\right|}{y_i^{obs}}\cdot 100\%, \quad (4)$$

$$MAE = \frac{1}{N}\sum_{i=1}^{N}\left|y_i^{est} - y_i^{obs}\right|, \quad (5)$$

$$RMSE = \sqrt{\frac{1}{N}\sum_{i=1}^{N}\left(y_i^{est} - y_i^{obs}\right)^2}, \quad (6)$$

where y_i^{est} and y_i^{obs} are the estimated and in situ measured values, respectively, and N is the number of match-ups.

3. Results and Discussion

3.1. Statistics of Chl a and TSS Variations

The descriptive statistics of the considered datasets for Chl *a* and TSS are given in Table 1, where *N* is the number of pixels with averaged measurements inside, and Min,

Max, and Mean are the minimum, maximum, and mean values of the arrays, respectively; Median is the median value, and STD is the standard deviation.

Table 1. Statistics of Chl *a* and TSS concentrations measured on 16 July 2022.

Parameter	N	Min	Max	Mean	Median	STD
Chl *a* (μg/L)	4111	0.032	0.952	0.328	0.293	0.201
TSS (mg/L)	1071	0.707	2.133	1.155	1.012	0.324

The resulting datasets for Chl *a* and TSS were randomly mixed (separately for each zone 1–7) and divided into two datasets: for calibration (~50%) and validation (~50%).

3.2. Reflectance Spectra

In order to control the quality of in-situ measured R_{rs}, in addition to visual analysis of in-situ radiometric radiances, where data with dramatic leaps were excluded from the analysis due to the sun glints or ship rotations, the Quality Water Index Polynomial (QWIP) score [42] was used in this work in order to remove low-quality Rrs. The QWIP's approach allows for control of the quality of hyperspectral water-leaving reflectance in terms of its spectral shape. The approach is based on a polynomial relation describing a well-proportioned trend for the Apparent Visible Wavelength (AVW), which is calculated as the weighted harmonic mean of the reflectance spectrum across a range of wavelengths, to anticipate a Normalized Difference Index (NDI) for the wavelengths of 492 and 665 nm. Finally, the difference between the calculated and predicted NDI should be calculated in order to obtain the QWIP score. The data with QWIP scores that exceeded the prescribed deviation from the polynomial relation, namely $+/-$ 0.2, were excluded from further analysis.

In Figure 7a, there are examples of hyperspectral in-situ measured R_{rs}, which were used for calibration and validation (passed QWIP quality control, QWIP score < |0.2|). Such spectra are typical for clear blue waters with high reflectance at shorter wavelengths and low reflectance for the NIR and red regions of the spectra. Chl *a* and TSS concentrations for such waters usually take values below 3 μg/L and 3 mg/L, respectively [43]. It can be seen that the obtained hyperspectral R_{rs} values correspond to the optical water properties of the high-altitude oligotrophic Issyk-Kul Lake. Additionally, the spectra excluded from the analyses (failed QWIP quality control, QWIP score > |0.2|) are shown in Figure 7b.

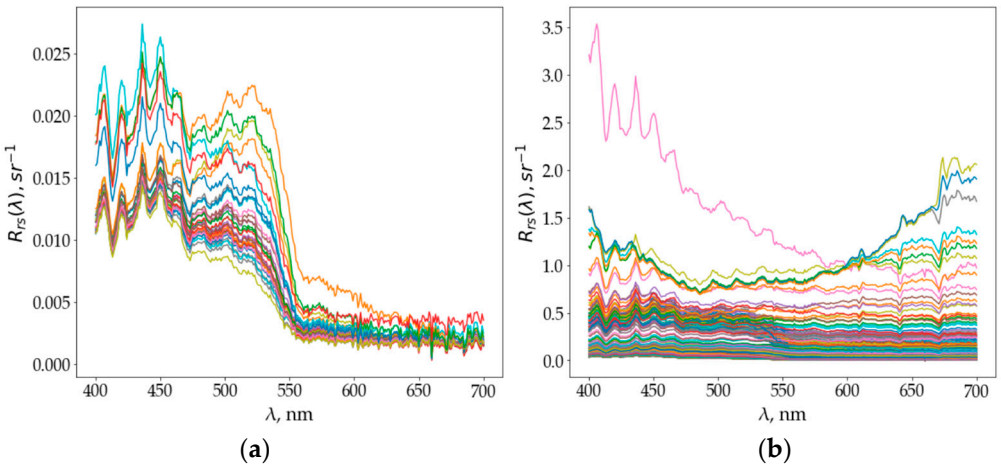

Figure 7. Examples of R_{rs} spectra measured in Lake Issyk-Kul on 16 July 2022: (**a**) spectra included in the temporal-synchronous dataset for calibration /validation of Chl *a* and TSS models; and (**b**) spectra excluded from the analysis.

3.3. Chl a Model

The development of the regional bio-optical model for Chl *a* was performed using calibration (2057 measurements) and validation (2054 measurements) datasets. The descriptive statistics of these datasets are shown in Table 2.

Table 2. Statistics describing the concentrations of Chl *a* (μg/L) of the calibration and validation dataset.

Dataset	N	Min	Max	Mean	Median	STD
Calibration	2057	0.036	0.952	0.328	0.293	0.202
Validation	2054	0.032	0.864	0.327	0.291	0.199
All	4111	0.032	0.952	0.328	0.292	0.201

Comparing the band ratios (B2/B3) and (B4/B5) for the matched Sentinel-2 data and in situ R_{rs}, the qualitative match was revealed for the blue-green bands; therefore, the OC2 algorithm (https://oceancolor.gsfc.nasa.gov/atbd/chlor_a/, accessed on 10 December 2022) calibrated by our data was employed for Chl *a* retrieval (Figure 8).

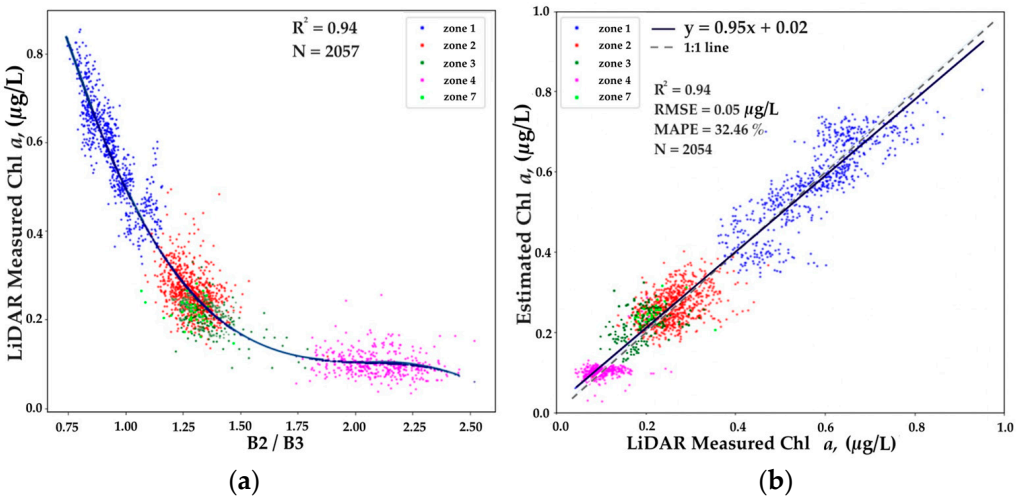

Figure 8. Results of (**a**) calibration (N = 2057) and (**b**) validation (N = 2054) of OC2 algorithm with coefficients a = [−0.3103; −2.3868; −3.7861; 17.8521; −13.8532] for Chl *a* in Issyk-Kul Lake. The colors of the dots correspond to the zones shown in Figure 6.

The validation result is a linear model with a high determination coefficient R^2 = 0.94 and an error value *MAPE* = 32.46%. The analysis showed that the high *MAPE* corresponded to data from the 4th clear water zone, where low Chl *a* concentrations prevailed (<0.2 μg/L). These low concentrations are well measured by LiDAR due to their high sensitivity, but the same cannot be said about Sentinel-2, where the variability is not observed (except for random noise). Thus, this zone with minimal concentrations could be excluded from consideration, but it illustrates the physics of measurements and clearly demonstrates the limitations of active and passive means of remote sensing.

3.4. TSS Model

Similar to Chl *a*, calibration (536 measurements) and validation (535 measurements) datasets were also used for creating regional TSS models. The descriptive statistics of these datasets are shown in Table 3.

Table 3. Statistics describing TSS concentrations (mg/L) of the calibration and validation dataset.

Dataset	N	Min	Max	Mean	Median	STD
Calibration	536	0.707	2.131	1.154	1.010	0.324
Validation	535	0.712	2.133	1.155	1.012	0.323
All	1071	0.707	2.133	1.155	1.012	0.324

A linear model based on the B3 band (560 nm) was chosen for TSS, which showed the best results with R^2 = 0.96, *RMSE* = 0.07 mg/L, and low *MAPE* = 6.07% (Figure 9).

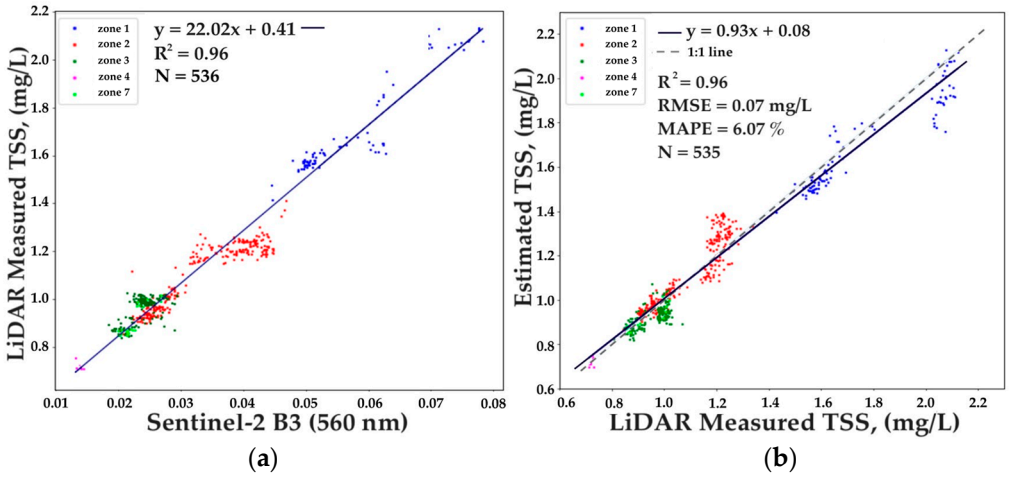

Figure 9. Results of (**a**) calibration (N = 536) and (**b**) validation (N = 535) of linear B3 algorithm (TSS = 22.02·B3 + 0.41) for TSS in Issyk-Kul Lake. The dashed line represents the 1:1 line.

3.5. Comparison of Conventional and Newly Developed Bio-Optical Models of Chl a and TSS

Having obtained qualitative results in the development of regional models for Chl *a* and TSS, we decided to compare how they differ from conventional models for each bio-optical parameter. We evaluated the accuracy of empirical models for Chl *a* based on the OC2 algorithm with coefficients for the OLI sensor, which are also applicable to MSI [44]:

$$log_{10}Chl\ a = a_0 + \sum_{i=1}^{4} a_i \cdot log_{10}\left(\frac{R_{rsblue}}{R_{rsgreen}}\right)^i \quad (7)$$

where $a = [0.1977; -1.8117; 1.9742; -2.5635; -0.7218]$.

For TSS, we evaluated the accuracy of the algorithm developed by Nechad [45], which is widely employed around the world due to its ability to adapt to different sensors and spectral bands [46]. It is based on the use of a single spectral band in the range from red to NIR (in our case, 665 nm) and is described by the equation

$$TSS = \frac{A_p(\lambda) \cdot \rho_w(\lambda)}{1 - \frac{\rho_w(\lambda)}{C_p(\lambda)}}, \quad (8)$$

where $\rho_w(\lambda)$ is the water-leaving reflectance in the red or NIR band, $A_p(\lambda)$ and $C_p(\lambda)$ are the sensor-specific coefficients calibrated for OLI and MSI (https://odnature.naturalsciences.be/remsem/acolite-forum, accessed on 20 December 2022) and equal to 342.10 and 0.19563, respectively. The obtained results are presented in Figure 10. It can be seen that the OC2 algorithm with NASA standard coefficients overestimates in situ Chl *a* concentrations by more than 3 times, while the Nechad algorithm for TSS also overestimates concentrations by a factor of 2–6.

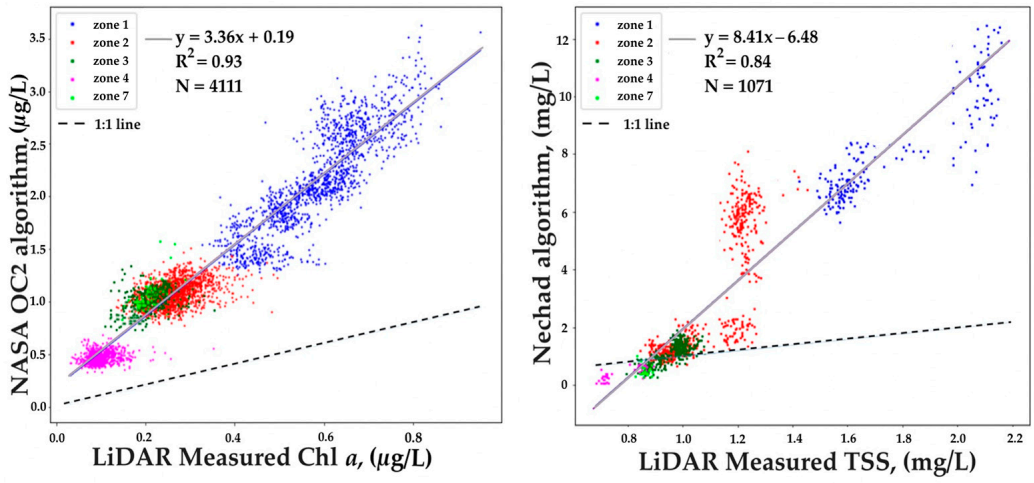

(**a**) (**b**)

Figure 10. Results of the comparison of (**a**) NASA OC2 standard algorithm for Chl *a* and (**b**) Nechad algorithm for TSS in Issyk-Kul Lake.

3.6. Chl a and TSS Mapping Using LIF LiDAR Data

In addition to satellite models, we also considered LiDAR maps of the spatial distribution of Chl *a* and TSS (Figure 11). In the central part of the lake, the concentrations of Chl *a* and TSS did not exceed 1 µg/L and 1.2 mg/L, respectively, which confirms the oligotrophic status of the lake. At the same time, inside the river mouths, the values of Chl *a* and TSS reached 2 µg/L and 10 mg/L, respectively, demonstrating an excess of lake values by almost an order of magnitude for TSS and several times for Chl *a*.

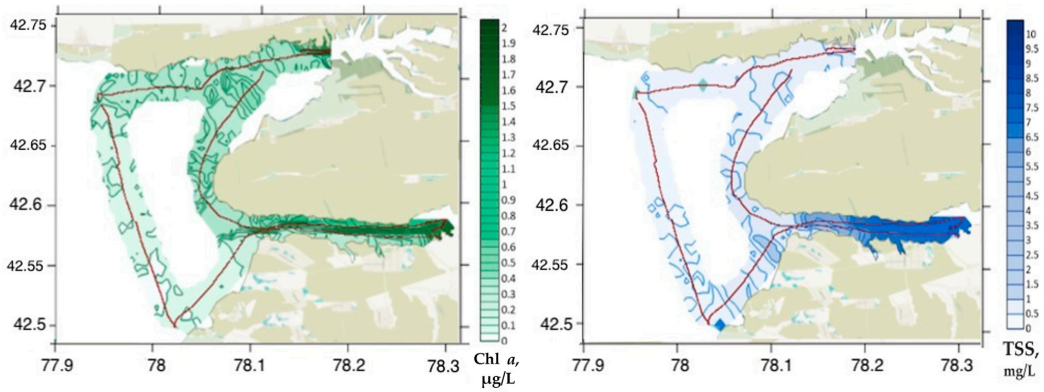

(**a**) (**b**)

Figure 11. Spatial distribution of (**a**) Chl *a* and (**b**) TSS in Issyk-Kul Lake on 16 July 2022 obtained by LiDAR.

Obviously, in order to obtain more relevant studies in the shore zone under the satellite overpass, it is advisable to use a faster vessel, reduce the time interval between the satellite overpass and in situ measurements, and increase the ship exploration area as much as possible to collect data with a wide range of variability. The above-mentioned errors can partly be explained by the rapid variability of the water quality parameters, primarily due to wind forcing. Figures 12 and 13 show significant changes in the concentrations of Chl *a* and TSS in the estuarine region of the Jergalan River for several hours under the influence of increasing wind, both for the day of measurement and for the next one.

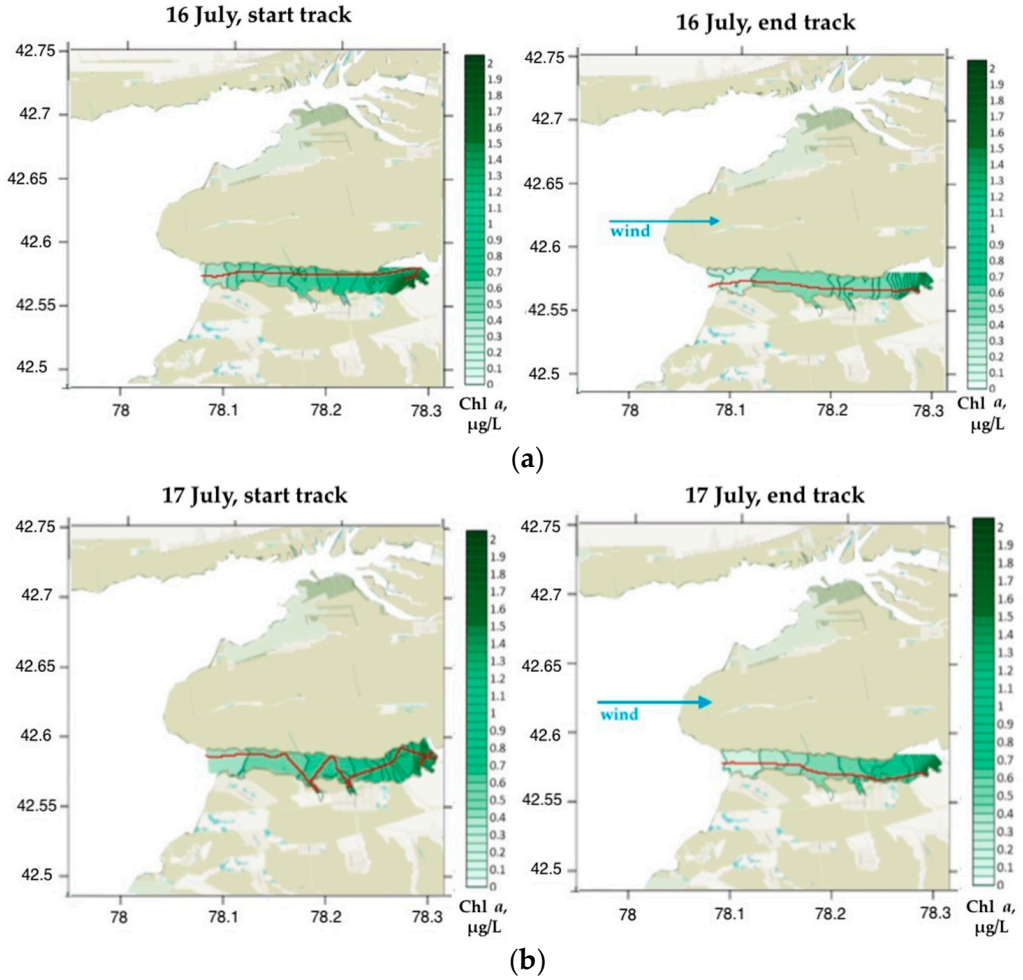

Figure 12. Spatial distribution of Chl *a* in Issyk-Kul Lake on the start and end tracks on (**a**) 16 July 2022 (from 8:50 to 09:50), and (**b**) 17 July 2022 (from 17:00 to 18:00).

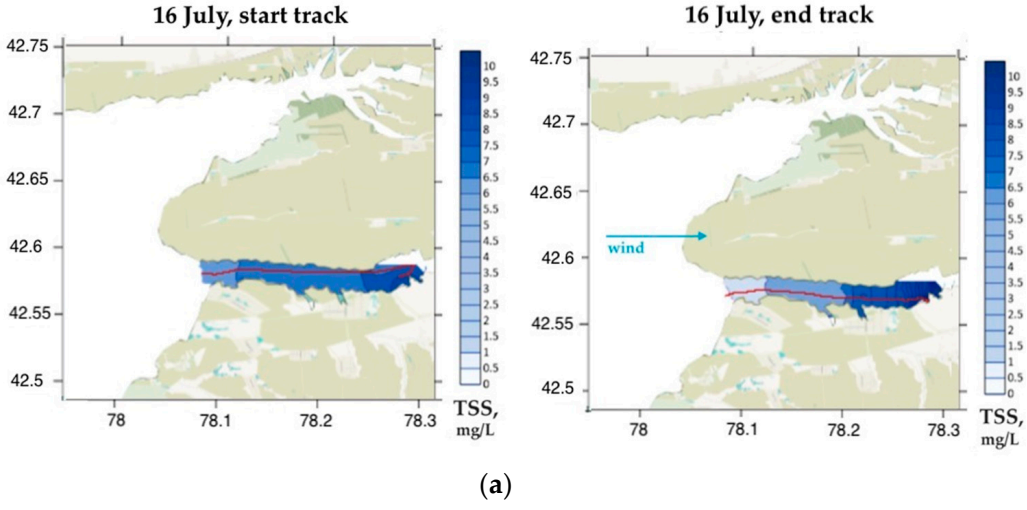

Figure 13. *Cont.*

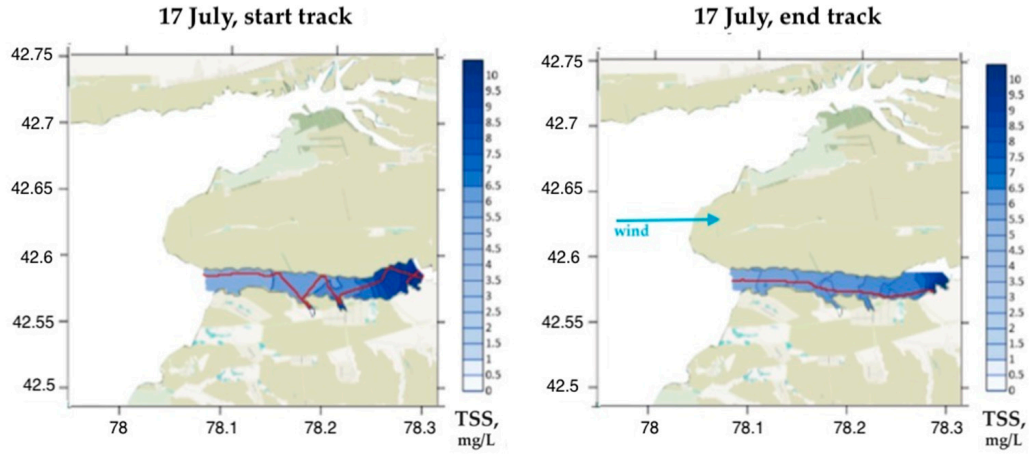

(**b**)

Figure 13. Spatial distribution of TSS in Issyk-Kul Lake on the start and end tracks on (**a**) 16 July 2022 (from 08:50 to 09:50), and (**b**) 17 July 2022 (from 17:00 to 18:00).

3.7. Chl a and TSS Mapping Using Sentinel-2 Data

The obtained regional models for Chl *a* and TSS were used for a preliminary assessment of the temporal variability of these parameters in the lake and tributaries during the year. No such studies had been carried out for Issyk-Kul Lake before. However, it is important to establish the characteristic ranges of variability as well as to determine the regions and dates of their manifestation. Such information is necessary not only to describe the lake dynamics but also to plan the next expeditions to develop new bio-optical models and refine the proposed ones.

For this purpose, we downloaded and analyzed 46 Sentintel-2 images of the study region from 1 January to 31 December 2022. Twelve of them, as illustrative images, are shown in Table 4. In the period from January to March, the main part of the studied region, including river mouths, was characterized by clear water (Table 4, images a–c). On some windy days, areas with an increased concentration of Chl *a* (4.6 µg/L) and TSS (2.8 mg/L) were observed along the northern coast in a narrow strip (about 1.1–1.2 km) and in shallow water near the mouth of the Jergalan River (Table 4, image b). The runoff of the Tyup and Jergalan Rivers appeared with the snow melting in the first week of April (Table 4, image d). The maximum runoff occurred in mid-April (Table 4, image e). The concentrations of TSS at the mouth of the Tyup River reached 4.0 mg/L, and in Jergalan, 3.1 mg/L, which was about 3–4 times higher than the winter background values. These inflows had manifestations as waters with increased turbidity along the entire northern shore in a much wider strip of 4 km than in the case of wind waves. The weakening of both rivers occurred during the month until the end of May (Table 4, image f). From that point, no notable variations in TSS concentrations in the Tyup River were observed until the end of the year. The behavior of the mouth of the Jergalan River and the southwest shore differed. On the one hand, the quasi-stable flow of the Jergalan River took place until the beginning of October, with a slight increase in rainfall days. On the other hand, a periodic runoff of small rivers with origins in the higher mountains, for example, the Irdyk and Karakol Rivers, as well as the Jeta-Oguz River south of the mouth of the Jergalan River (Table 4, images g, h) takes place. A relatively regular manifestation of these runoffs was observed in the first half of summer due to the snow melting in the mountains. Later, these runoffs and the behavior of the Jergalan River correlated with rainy days. By November, the contribution of all rivers was leveled, and areas with increased turbidity were absent, as at the beginning of winter, which was discussed above. At the same time, in the period from November to December, there were days of very strong and continuous northern winds (about 20–30 m/s). Table 4, images j and k show examples of shore erosion by intense waves and the transfer of water masses with a high concentration of TSS (up to 2.4 mg/L)

to the central part of the considered water area, where they were not previously observed throughout the year.

Table 4. RGB-composition of the Sentinel-2/MS images (**left column**) and spatial distribution of Chl *a* (**center column**) and TSS (**right column**) in Issyk-Kul Lake, obtained using the proposed regional bio-optical models.

Sentinel-2 Image	Chl *a* Maps	TSS Maps
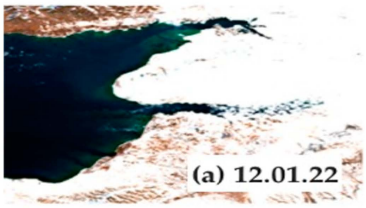	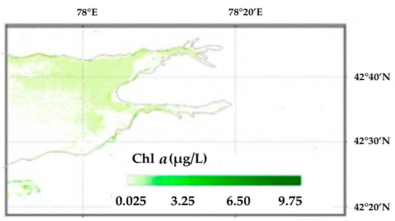	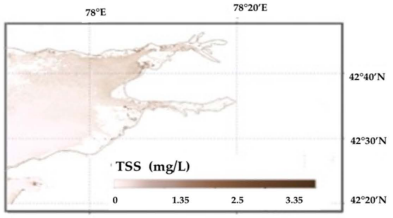
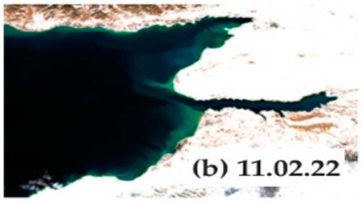	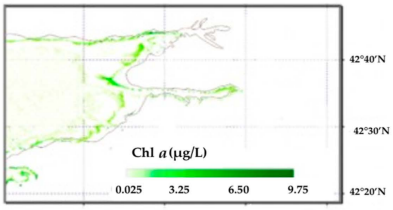	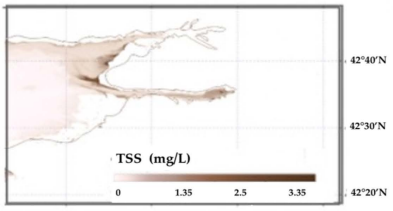
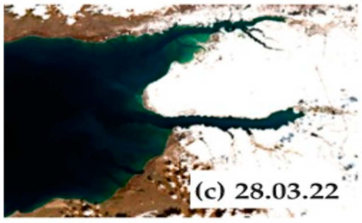	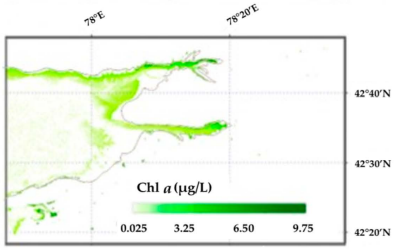	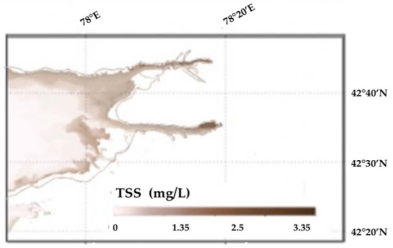
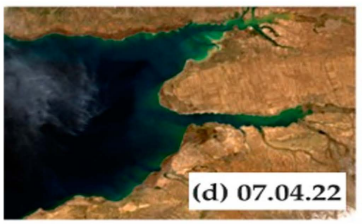	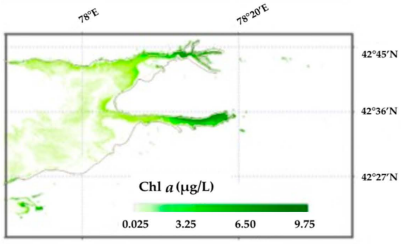	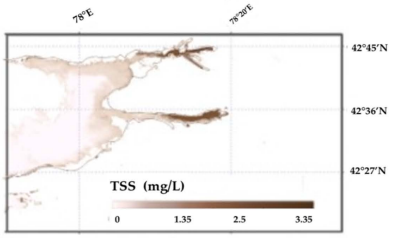
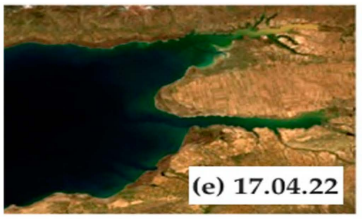	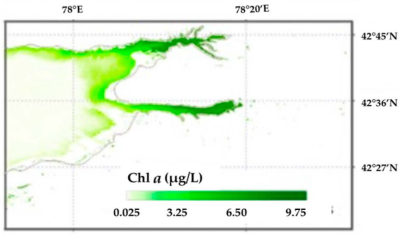	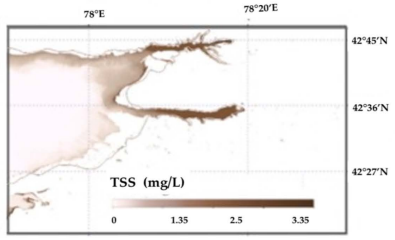
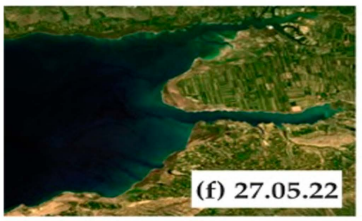	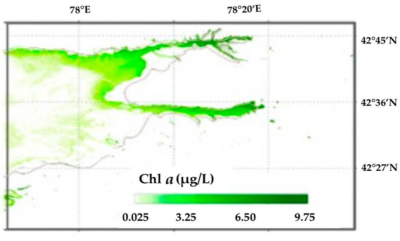	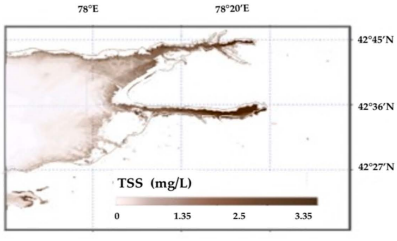

Table 4. *Cont.*

Sentinel-2 Image	Chl *a* Maps	TSS Maps
(g) 16.07.22	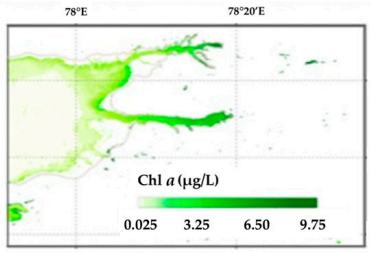	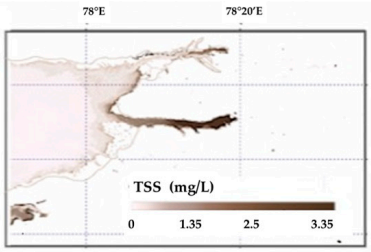
(h) 20.08.22	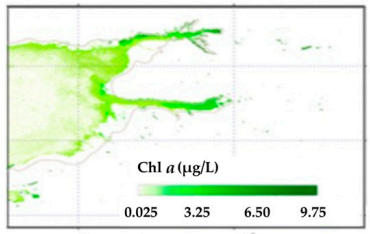	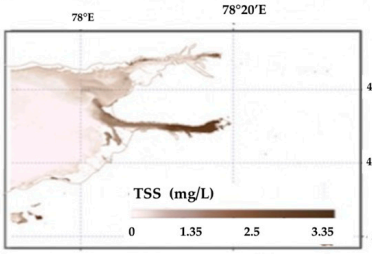
(i) 13.11.22	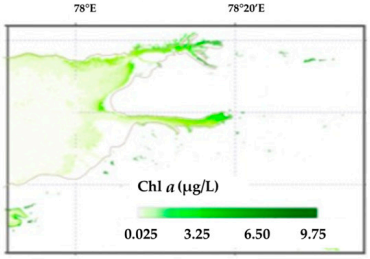	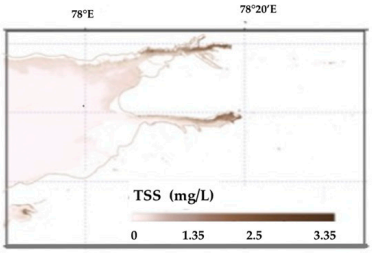
(j) 18.11.22	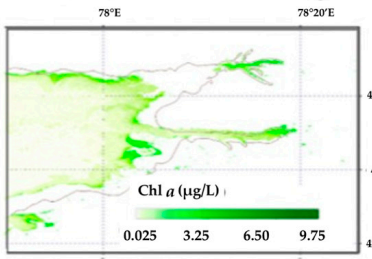	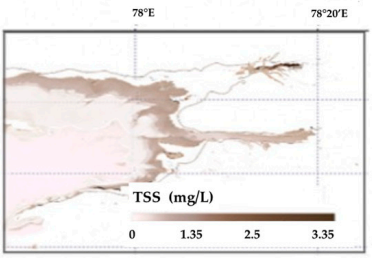
(k) 28.11.22	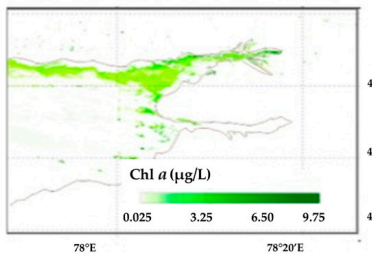	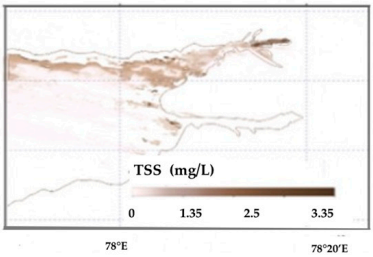
(l) 03.12.22	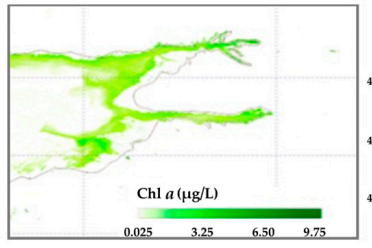	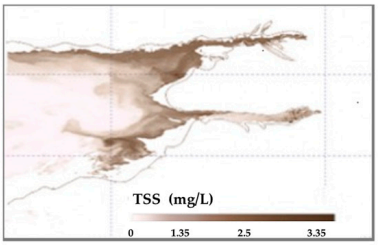

In addition to the RGB-composite images of the lake, the right column in Table 4 contains the distribution of Chl *a* and TSS in weight units, reconstructed according to the proposed bio-optical models. The shallow water zone is camouflaged. For this, the

following assumption was used. The satellite ocean color sensors can only sense a water column up to one optical depth [47]. One optical depth is the depth where the total irradiance is about 37% of the total surface irradiance, and for clear waters, it does not exceed 50 m, while it can be equal to a few centimeters for muddy waters. If the depth of the lake in shallow water becomes less than the optical depth, the satellite sensor can detect the bottom.

Therefore, it was decided to exclude shallow areas from mapping. For this purpose, we selected the image with visually clear waters across all areas in the studied region (it was the image dated 13 November 2022, in Table 4) and considered the green band B3 (560 nm) in SNAP software. Furthermore, in terms of radiance, we analyzed where the bottom relief in the shore area of the lake was visible and applied a mask to it. Due to the different turbidity conditions of the water on different days, the bottom mask for each image was selected separately; thus, the radiance limits were different depending on the satellite overpass date.

Based on the obtained results (Table 4), it is possible to observe maxima of Chl *a* and TSS concentrations everywhere in the studied region. Depending on the time of year, the concentrations varied, i.e., maximum values for the spring and summer months were more than 6 μg/L for Chl *a* and more than 3 mg/L for TSS, where maximum values in late autumn and winter were 2.2 μg/L for Chl *a* and 2.0 mg/L for TSS. It is worth noting that in the summer, bright blooms were observed in satellite images, especially in the area of the Jergalan River, which excludes the effect of shallow water on the signals recorded by optical scanners. The detailed information regarding the concentrations of Chl *a* and TSS for all the mentioned dates is shown in Table 5.

Table 5. Sub-annual variations of Chl *a* and TSS concentrations in 2022 obtained using the presented regional bio-optical models.

Image	Date	Max Chl *a* (μg/L)	Min Chl *a* (μg/L)	Max TSS (mg/L)	Min TSS (mg/L)
a	12 January 2022	2.2	0.01	2.2	0.11
b	11 February 2022	3.5	0.01	2.8	0.11
c	28 March 2022	5.0	0.01	2.1	0.12
d	7 April 2022	6.5	0.01	3.6	0.10
e	17 April 2022	6.6	0.01	4.0	0.11
f	27 May 2022	6.6	0.01	3.4	0.10
g	16 July 2022	6.2	0.01	3.6	0.12
h	20 August 2022	6.2	0.02	3.2	0.11
i	13 November 2022	2.2	0.01	2.1	0.10
j	18 November 2022	2.3	0.02	2.4	0.10
k	28 November 2022	2.4	0.01	2.0	0.11
l	3 December 2022	2.3	0.01	2.2	0.11

4. Conclusions

Based on one day of in situ measurements, we conclude that the methodology proposed by our team for the development of regional bio-optical models and algorithms for interpreting satellite data on the watercolor has good applicability not only for eutrophic waters (as shown before) but also for oligotrophic waters.

Measurements using LiDAR from a moving vessel make it possible to obtain about 15,000 measurements near the time of the satellite overpass (within ±1 h). This is the main advantage of this approach compared to station measurements. This allows, on the one hand, studying the spatiotemporal variability of the optically active components of natural water and, on the other hand, measuring bio-optical properties in wide (close to natural distribution) ranges over large areas. A large number of measurements allow filtering out some of them without significant damage to the accuracy of the calibration of bio-optical models, for example, in cases of cloudiness in the measurement area or incorrect data. If measurements were traditionally made at stations, such data would simply be

lost. To develop a bio-optical model based on measurements at the stations, dozens of expeditions are required to collect a comparable number of ground truth data points. In the case of measurements from a moving vessel, the number of comparison pairs (R_{rs} via the concentration of the water constituents) is large enough to calibrate and validate bio-optical algorithms with high accuracy, even for one satellite image (one expedition day). Of course, there is also a negative point, i.e., the temporal variability of characteristics is not taken into account. Besides, our goal was to demonstrate the novel measurement technique and the capability of its application for monitoring a distinct oligotrophic water body for its further development and improvement. Creating all-season models, which also take into account various climatic and regional features of the lake and are verified for its different regions, requires a series of one-day but repetitive subsatellite experiments in the important parts of the lake (if it is large enough) at different times of the year under different weather conditions (first of all, at a different intensity of water inflows). This will make it possible to draw a reasonable conclusion about the suitability and universality of the new regional models for relevant and operational environmental satellite monitoring. At the same time, there is the possibility of retrospective analysis of archival satellite measurement data, as well as a theoretical transition from modern color scanners to the earliest, such as MODIS and SeaWiFS. For this purpose, it is necessary to use periods of simultaneous overpasses by different satellite ocean color sensors, which will enable one to analyze the full-time array of satellite data for the studied water region.

The proposed methodology and instrumentation provide an opportunity to develop and validate new regional satellite bio-optical models for future satellite missions, more and more of which are being put into operation every year. However, first of all, it is necessary to organize a full-fledged scientific study on the inter-seasonal study of Lake Issyk-Kul using the proposed method to establish regular environmental monitoring of this unique natural object.

Author Contributions: Conceptualization, S.A., V.P. and A.M.; methodology, V.P., A.M. and S.F.; software, E.K. and S.F.; validation, V.P., E.K., S.F. and B.K.; data curation, E.K.; writing—original draft preparation, V.P., A.M. and E.K.; writing—review and editing, V.P., A.M., E.K. and S.F.; visualization, E.K. and M.A.; supervision, S.A.; project administration, S.A.; funding acquisition, K.J. All authors have read and agreed to the published version of the manuscript.

Funding: The research was funded by: the Russian Hydrometeorological Service (Agreement No. 169-15-2023-002) regarding the field ground-truth LiDAR application methodology, all the data collection and validation; the Ministry of Education and Science of the Russian Federation (theme No. FFUF-2021-0006 regarding the development of radiophysical methods for studying the ocean and inland waters); the Federal Academic Leadership Program "Priority-2030" of Lobachevsky State University of Nizhny Novgorod (theme No. N-468-99_2021–2023 regarding the creating of regional bio-optical models).

Data Availability Statement: Data is unavailable due to privacy.

Acknowledgments: The authors thank "AVIA TRAFFIC" Ltd. and personally the Alik Askarov for the provision of air travel. We are grateful to Lev Yakushkin for his help with data collection in the field. The authors also thank the anonymous reviewers for their useful comments and suggestions.

Conflicts of Interest: The authors declare no conflict of interest or state.

Appendix A

This section provides some results of the accuracy assessment of Sentinel-2/MSI Level-2 radiance products (https://scihub.copernicus.eu, accessed on 20 November 2022). Figure A1 shows the time series of R_{rs} on 490 nm and 560 nm bands, which were used to develop bio-optical models. Scatterplots for R_{rs} are given in Figure A2. Some accuracy metrics for satellite R_{rs} (slope, intercept, Pearson coefficient (R), bias, RMSE, MAPE) are given in Table A1.

Several conclusions can be drawn. First, the accuracy of atmospheric correction (Sen2Cor) varies for different spectral bands. Second, there is a high correlation between the satellite and measured reflectances in the blue, green, and red range (Pearson coefficient 0.81–0.98). At the red range and the NIR (705 and 740 nm) bands, the correlation significantly worsens. Third, the presence of linearity between satellite and measured reflectances on 490 and 560 nm bands allows us to use them for the development of bio-optical algorithms.

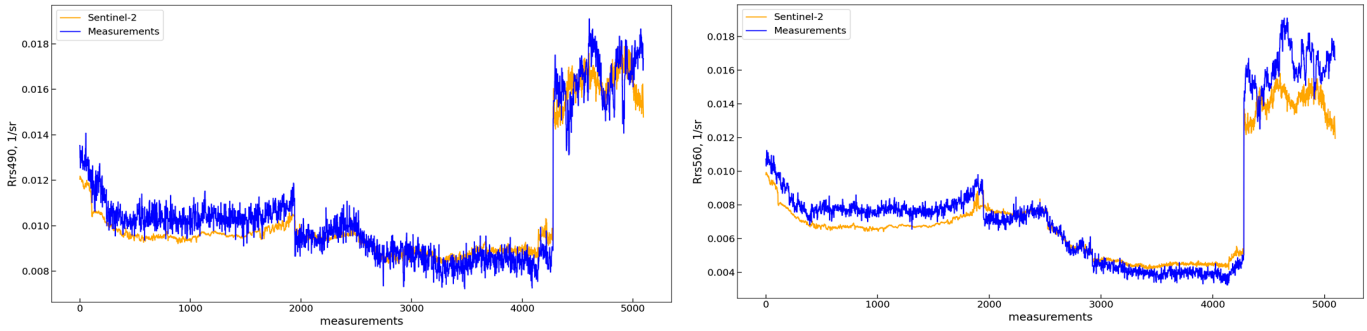

Figure A1. Remote-sensing reflectance on bands 490 nm (**a**) and 560 nm (**b**). Blue lines are measured reflectance, orange ones—satellite retrieved reflectance.

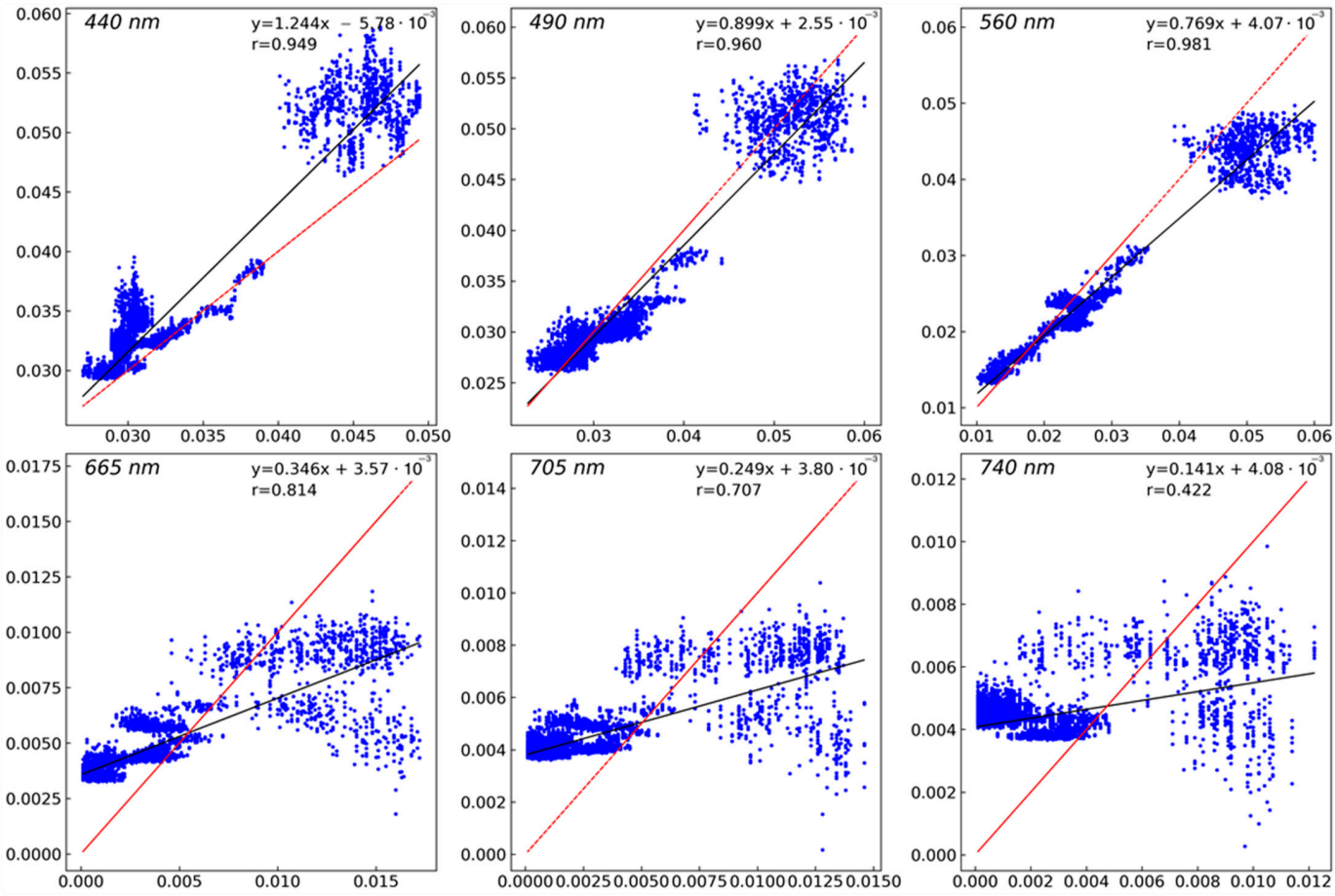

Figure A2. Satellite retrieved remote-sensing reflectance (y-axes) against measured remote-sensing reflectance (x-axes) for different spectral bands.

The low accuracy of the satellite R_{rs} retrieved using Sen2Cor in the red and NIR bands (3–5 times higher than the measured R_{rs}) is probably due to the lack of correction for sun glint and adjacency effects (which are strongly manifested in the red region of the spectrum). To obtain more accurate values, it is necessary to use an AC algorithm that takes into account these effects more accurately.

Table A1. Accuracy metrics.

Metrics/Wavelength	440	490	560	665	705	740
Slope	1.2444	0.899	0.7693	0.3461	0.2487	0.1413
Intercept	−0.0058	0.0026	0.0041	0.0036	0.0038	0.0041
R	0.949	0.96	0.981	0.814	0.707	0.422
RMSE	0.0036	0.0026	0.0039	0.003	0.0029	0.0029
bias	0.0024	−0.0009	−0.0018	0.0008	0.0012	0.0016
MAPE	7.0	6.0	10.9	225.1	270.5	368.6

References

1. Toming, K.; Kutser, T.; Laas, A.; Sepp, M.; Paavel, B.; Nõges, T. First Experiences in Mapping Lake Water Quality Parameters with Sentinel-2 MSI Imagery. *Remote Sens.* **2016**, *8*, 640. [CrossRef]
2. Molkov, A.A.; Fedorov, S.V.; Pelevin, V.V.; Korchemkina, E.N. Regional Models for High-Resolution Retrieval of Chlorophyll *a* and TSS Concentrations in the Gorky Reservoir by Sentinel-2 Imagery. *Remote Sens.* **2019**, *11*, 1215. [CrossRef]
3. Dörnhöfer, K.; Göritz, A.; Gege, P.; Pflug, B.; Oppelt, N. Water constituents and water depth retrieval from Sentinel-2a—A first evaluation in an oligotrophic lake. *Remote Sens.* **2016**, *8*, 941. [CrossRef]
4. Pahlevan, N.; Smith, B.; Schalles, J.; Binding, C.; Cao, Z.; Ma, R.; Alikas, K.; Kangro, K.; Gurlin, D.; Hà, N.; et al. Seamless Retrievals of Chlorophyll-a from Sentinel-2 (MSI) and Sentinel-3 (OLCI) in Inland and Coastal Waters: A Machine-Learning Approach. *Remote Sens. Environ.* **2020**, *240*, 111604. [CrossRef]
5. Palmer, S.; Hunter, P.; Lankester, T.; Hubbard, S.; Spyrakos, E.; Tyler, A.; Présing, M.; Horváth, H.; Lamb, A.; Balzter, H.; et al. Validation of Envisat MERIS Algorithms for Chlorophyll Retrieval in a Large, Turbid and Optically Complex Shallow Lake. *Remote Sens. Environ.* **2014**, *5*, 157. [CrossRef]
6. Pelevin, V.; Zlinszky, A.; Khimchenko, E.; Toth, V. Ground truth data on Chlorophyll-a, chromophoric dissolved organic constituents and suspended sediment concentrations in the upper water layer as obtained by LIF LiDARat high spatial resolution. *Int. J. Remote Sens.* **2017**, *38*, 1967–1982. [CrossRef]
7. Zavialov, P.; Izhitskiy, A.; Kirillin, G.; Khan, V.; Konovalov, B.; Makkaveev, P.; Pelevin, V.; Rimskiy-Korsakov, N.; Alymkulov, S.; Zhumaliev, K. New profiling and mooring records help to assess variability of Lake Issyk-Kul and reveal unknown features of its thermohaline structure. *Hydrol. Earth Syst. Sci.* **2018**, *22*, 6279–6295. [CrossRef]
8. Zavyalov, P.O.; Zhumaliev, K.M.; Alymkulov, S.A.; Konovalov, B.V.; Makkaveev, P.N.; Pelevin, V.V.; Rimsky-Korsakov, N.A.; Izhitsky, A.S.; Izhitskaya, E.S. *Comprehensive Studies of Lake Issyk-Kul: Part 1*; Kyrgyz-Russian Slavic University: Bishkek, Kyrgyzstan, 2018; p. 194. (In Russian)
9. Romanovsky, V.V. *Lake Issyk-Kul as a Natural Complex*; Frunze: Ilim, Russia, 1991; p. 169. (In Russian)
10. Zavialov, P.O.; Pelevin, V.V.; Belyaev, N.A.; Izhitskiy, A.S.; Konovalov, B.V.; Krementskiy, V.V.; Goncharenko, I.V.; Osadchiev, A.A.; Soloviev, D.M.; Garcia, C.A.E.; et al. High resolution LiDARmeasurements reveal fine internal structure and variability of sediment-carrying coastal plume. *Estuar. Coast. Shelf Sci.* **2018**, *205*, 40–45. [CrossRef]
11. Zavyalov, P.O.; Alymkulov, S.A.; Zhumaliev, K.M.; Israilova, N.A.; Konovalov, B.V.; Sapozhnikov, F.V.; Makkaveev, P.N.; Khan, V.M.; Pelevin, V.V.; Izhitsky, A.S.; et al. *Comprehensive Studies of Lake Issyk-Kul: Part 2*; Kyrgyz-Russian Slavic University: Bishkek, Kyrgyzstan, 2020; p. 208. (In Russian)
12. Pereira-Sandoval, M.; Ruescas, A.B.; García-Jimenez, J.; Blix, K.; Delegido, J.; Moreno, J. Supervised Classifications of Optical Water Types in Spanish Inland Waters. *Remote Sens.* **2022**, *14*, 5568. [CrossRef]
13. Vanderhoof, M.K.; Alexander, L.; Christensen, J.; Solvik, K.; Nieuwlandt, P.; Sagehorn, M. High-frequency time series comparison of Sentinel-1 and Sentinel-2 satellites for mapping open and vegetated water across the United States (2017–2021). *Remote Sens. Environ.* **2023**, *288*, 113498. [CrossRef] [PubMed]
14. Many, G.; Escoffier, N.; Ferrari, M.; Jacquet, P.; Odermatt, D.; Mariethoz, G.; Perolo, P.; Perga, M.-E. Long-Term Spatiotemporal Variability of Whitings in Lake Geneva from Multispectral Remote Sensing and Machine Learning. *Remote Sens.* **2022**, *14*, 6175. [CrossRef]
15. Balasubramanian, S.V.; Pahlevan, N.; Smith, B.; Binding, C.; Schalles, J.; Loisel, H.; Gurlin, D.; Greb, S.; Alikas, K.; Randla, M.; et al. Robust algorithm for estimating total suspended solids (TSS) in inland and nearshore coastal waters. *Remote Sens. Environ.* **2020**, *246*, 111768. [CrossRef]

16. Jiang, Y.-J.; He, W.; Liu, W.-X.; Qin, N.; Ouyang, H.-L.; Wang, Q.-M.; Kong, X.-Z.; He, Q.-S.; Yang, C.; Yang, B. The seasonal and spatial variations of phytoplankton community and their correlation with environmental factors in a large eutrophic Chinese lake (Lake Chaohu). *Ecol. Indic.* **2014**, *40*, 58–67. [CrossRef]
17. Wynne, T.T.; Stumpf, R.P. Spatial and temporal patterns in the seasonal distribution of toxic cyanobacteria in western Lake Erie from 2002–2014. *Toxins* **2015**, *7*, 1649–1663. [CrossRef] [PubMed]
18. Hansen, C.H.; Burian, S.J.; Dennison, P.E.; Williams, G.P. Spatiotemporal Variability of Lake Water Quality in the Context of Remote Sensing Models. *Remote Sens.* **2017**, *9*, 409. [CrossRef]
19. Pelevin, V.; Zavialov, P.; Konovalov, B.; Zlinszky, A.; Palmer, S.; Toth, V.; Goncharenko, I.; Khymchenko, L.; Osokina, V. Measurements with high spatial resolution of Chlorophyll-a, CDOM and total suspended constituents in coastal zones and inland water basins by the portable UFL Lidar. In Proceedings of the 35th EARSeL Symposium—European Remote Sensing: Progress, Challenges and Opportunities, Stockholm, Sweden, 15–19 June 2015.
20. Hoge, F.E.; Lyon, P.E.; Swift, R.N.; Yungel, J.K.; Abbott, M.R.; Letelier, R.M.; Esaias, W.E. Validation of Terra-MODIS phytoplankton chlorophyll fluorescence line height. I. Initial airborne LiDARresults. *Appl. Opt.* **2003**, *42*, 2767–2771. [CrossRef]
21. Aibulatov, N.A.; Zavialov, P.O.; Pelevin, V.V. Some Features of Self-Purification of Russian Black Sea Shoaling Waters near River Entries. *Geosci. Ecol.* **2008**, *4*, 301–310.
22. Vasilescu, J.; Onciu, T.; Jugaru, L.; Belegante, L. Remote estimation of fluorescence marine components distribution. *Rom. Rep. Phys.* **2009**, *61*, 721–729.
23. Cisek, M.; Colao, F.; Demetrio, E.; Di Cicco, A.; Drozdowska, V.; Goszczko, I.; Fiorani, L.; Lazic, V.; Okladnikov, I.G.; Palucci, A.; et al. Remote and local monitoring of dissolved and suspended fluorescent organic matter off the Svalbard. *J. Optoelectron. Adv. Mater.* **2010**, *12*, 1604.
24. Pelevin, V.V.; Zavjalov, P.O.; Belyaev, N.A.; Konovalov, B.V.; Kravchishina, M.D.; Mosharov, S.A. Spatial variability of concentrations of chlorophyll a, dissolved organic matter and suspended particles in the surface layer of the Kara Sea in September 2011 from LiDAR data. *Oceanology* **2017**, *57*, 165–173. [CrossRef]
25. Drozdowska, V. The LiDAR investigation of the upper water layer fluorescence spectra of the Baltic Sea. *Eur. Phys. J. Spec. Top.* **2007**, *144*, 141–145. [CrossRef]
26. Barbini, R.; Colao, F.; Fantoni, R.; L Fiorani, L.; Palucci, A. Remote sensing of the Southern Ocean: Techniques and results. *J. Optoelectron. Adv. Mater.* **2001**, *3*, 817–830.
27. Zavialov, P.O.; Kopelevich, O.V.; Kremenetskiy, V.V.; Pelevin, V.V.; Grabovskiy, A.B.; Gureev, B.A.; Grigoriev, A.V.; Peresypkin, V.I.; Ding, C.F.; Hsu, M.H. A joint Russian-Taiwanese expedition at the shelf of the South China Sea: Searching for manifestations of groundwater discharge to the ocean. *Oceanology* **2010**, *50*, 618–622. [CrossRef]
28. Zavialov, P.O.; Barbanova, E.S.; Pelevin, V.V.; Osadchiev, A.A. Estimating the deposition of river-borne suspended matter from the joint analysis of suspension concentration and salinity. *Oceanology* **2015**, *55*, 832–836. [CrossRef]
29. Collister, B.L.; Zimmerman, R.C.; Sukenik, C.I.; Hill, V.J.; Balch, W.M. Remote sensing of optical characteristics and particle distributions of the upper ocean using shipboard lidar. *Remote Sens. Environ.* **2018**, *215*, 85–96. [CrossRef]
30. Palmer, S.C.J.; Pelevin, V.V.; Goncharenko, I.; Kovács, A.W.; Zlinszky, A.; Présing, M.; Horváth, H.; Nicolás-Perea, V.; Balzter, H.; Tóth, V.R. Ultraviolet fluorescence LiDAR(UFL) as a measurement tool for water quality parameters in turbid lake conditions. *Remote Sens.* **2013**, *5*, 4405–4422. [CrossRef]
31. Chen, P.; Pan, D.; Wang, T.; Mao, Z.; Zhang, Y. Coastal and inland water monitoring using a portable hyperspectral laser fluorometer. *Mar. Pollut. Bull.* **2017**, *119*, 153–161. [CrossRef] [PubMed]
32. Duan, Z.; Li, Y.; Wang, J.; Zhao, G.; Svanberg, S. Aquatic environment monitoring using a drone-based fluorosensor. *Appl. Phys. B* **2019**, *125*, 108. [CrossRef]
33. Fiorani, L.; Barbini, R.; Colao, F.; De Dominicis, L.; Fantoni, R.; Palucci, A.; Artamonov, E.S. Combination of lidar, MODIS and SEAWIFS sensors for simultaneous chlorophyll monitoring. *EARSeL eProc.* **2004**, *3*, 8–17.
34. Fiorani, L.; Fantoni, R.; Lazzara, L.; Nardello, I.; Okladnikov, I.G.; Palucci, A. LiDAR calibration of satellite sensed CDOM in the Southern Ocean. *EARSeL eProc.* **2006**, *5*, 89–99.
35. Li, X.; Zhao, C.; Ma, Y.; Liu, Z. Field experiments of multi-channel oceanographic fluorescence LiDAR for oil spill and chlorophyll-a detection. *J. Ocean. Univ. China* **2014**, *13*, 597–603. [CrossRef]
36. Molkov, A.A.; Pelevin, V.V.; Korchemkina, E.N. Approach of non-station-based in situ measurements for high resolution satellite remote sensing of productive and highly changeable inland waters. *Fundam. Appl. Hydrophys.* **2020**, *13*, 60–67. [CrossRef]
37. Mueller, J.L.; Pietras, C.; Hooker, S.B.; Austin, R.W.; Miller, M.; Knobelspiesse, K.D.; Frouin, R.; Holben, B.; Voss, K. *Ocean Optics Protocols for Satellite Ocean Color Sensor Validation, Revision 4, Volume II: Instrument Specifications, Characterization and Calibration*; NASA/TM-2003-21621/Rev-Vol II; Goddard Space Flight Space Center: Greenbelt, MD, USA, 2003; pp. 1–56.
38. SCOR-UNESCO. Report of SCOR-UNESCO working group 17 on determination of photosynthetic pigments in Sea Water. In *Monograph of Oceanography Methodology*; UNESCO: Paris, France, 1966; Volume 1, pp. 9–18.
39. Konovalov, B.V.; Kravchishina, M.D.; Belyaev, N.A.; Novigatsky, A.N. Determination of the concentration of mineral particles and suspended organic substance based on their spectral absorption. *Oceanology* **2014**, *54*, 660–667. [CrossRef]
40. Mueller, J.L.; Bidigare, R.R.; Trees, C.; Balch, W.M.; Dore, J.; Drapeau, D.T.; Karl, D.; Van Heukelem, L.; Perl, J. *Ocean Optics Protocols for Satellite Ocean Color Sensor Validation, Revision 5, Volume 5: Biogeochemical and Bio-Optical Measurements and Data Analysis Protocols*; Goddard Space Flight Space Center: Greenbelt, MD, USA, 2003; pp. 5–24.

41. Mobley, C.D. Estimation of the remote sensing reflectance from above–water methods. *Appl. Opt.* **1999**, *38*, 7442–7455. [CrossRef] [PubMed]
42. Dierssen, H.M.; Vandermeulen, R.A.; Barnes, B.B.; Castagna, A.; Knaeps, E.; Vanhellemont, Q. QWIP: A Quantitative Metric for Quality Control of Aquatic Reflectance Spectral Shape Using the Apparent Visible Wavelength. *Front. Remote Sens.* **2022**, *3*, 869611. [CrossRef]
43. Spyrakos, E.; O'Donnell, R.; Hunter, P.D.; Miller, C.; Scott, M.; Simis, S.G.H.; Neil, C.; Barbosa, C.C.F.; Binding, C.E.; Bradt, S.; et al. Optical types of inland and coastal waters. *Limnol. Oceanogr.* **2018**, *63*, 846–870. [CrossRef]
44. Franz, B.A.; Bailey, S.W.; Kuring, N.; Werdell, P.J. Ocean color measurements with the Operational Land Imager on Landsat-8: Implementation and evaluation in SeaDAS. *J. Appl. Remote Sensing.* **2015**, *9*, 096070. [CrossRef]
45. Nechad, B.; Ruddick, K.G.; Park, Y. Calibration and Validation of a Generic Multisensor Algorithm for Mapping of Total Suspended Matter in Turbid Waters. *Remote Sens. Environ.* **2010**, *114*, 854–866. [CrossRef]
46. Odermatt, D.; Gitelson, A.; Brando, V.E.; Schaepman, M. Review of Constituent Retrieval in Optically Deep and Complex Waters from Satellite Imagery. *Remote Sens. Environ.* **2012**, *118*, 116–126. [CrossRef]
47. Morel, A.; Huot, Y.; Gentili, B.; Werdell, P.J.; Hooker, S.B.; Franz, B.A. Examining the consistency of products derived from various ocean color sensors in open ocean (Case 1) waters in the perspective of a multi-sensor approach. *Remote Sens. Environ.* **2007**, *111*, 69–88. [CrossRef]